



In-situ assembled S-scheme heterojunction of CsPbBr_3 nanocrystals and $\text{W}_{18}\text{O}_{49}$ ultrathin nanowires for enhanced bifunctional photocatalysis

Xinyan Jiang^a, Zhihao Chen^a, Yang Shu^a, Ahmed Mahmoud Idris^{b,*}, Sheng Li^{b,c}, Baojin Peng^{b,c}, Jin Wang^{a,c}, Zhengquan Li^{a,c, **}

^a Key Laboratory of the Ministry of Education for Advanced Catalysis Materials, Zhejiang Normal University, Jinhua, Zhejiang 321004, China

^b Zhejiang Normal University School of Physics and Electronic Information Engineering, Jinhua, Zhejiang 321004, China

^c Zhejiang Institute of Photoelectronic, Zhejiang Normal University, Jinhua, Zhejiang 321004, China



ARTICLE INFO

Keywords:

Heterojunctions
Photocatalysts
S-scheme
 CO_2 reduction
Toluene oxidation

ABSTRACT

Coupling CO_2 reduction with selective organic hydrocarbon oxidation using semiconductor photocatalysts holds significant importance in achieving carbon neutrality and obtaining valuable chemical raw materials. Nevertheless, finding a potential single photocatalyst with sufficient redox potentials capable of simultaneously driving redox reactions poses a formidable challenge. Herein, a distinct heterostructure of $\text{W}_{18}\text{O}_{49}/\text{CsPbBr}_3$ was meticulously fabricated through the *in-situ* growing of CsPbBr_3 nanocrystal on bundle-like $\text{W}_{18}\text{O}_{49}$ ultrathin nanowires *via* the hot-injection method. Experimental and theoretical characterizations reveal the establishment of a solid internal electric field at the heterojunction interface, enabling spatial charge separation *via* a valid interfacial S-scheme with strong redox ability. The $\text{W}_{18}\text{O}_{49}/\text{CsPbBr}_3$ heterostructure demonstrated decent performance, yielding high production of CO ($143 \mu\text{mol g}^{-1} \text{h}^{-1}$) and selective oxidizing toluene to benzaldehyde ($1546 \mu\text{mol g}^{-1} \text{h}^{-1}$) with an 80% selectivity. This work may pave a rational way for fully exploiting the potentials of photogenerated carriers in the heterojunction photocatalysts in synergistic photocatalytic systems.

1. Introduction

Photocatalytic reduction of CO_2 to solar fuels is a promising strategy to boost energy supply and cut greenhouse gas emissions [1–5]. In this process, H_2O oxidation serves as an ideal complement to the CO_2 reduction reaction [6,7]. However, the H_2O oxidation process is energy-intensive, requiring a four-electron transfer that is endothermic, thereby limiting the overall efficiency of the system [8,9]. Moreover, the oxidation of organic compounds offers an alternative route for organic synthesis characterized by mild conditions and high selectivity, surpassing conventional chemical routes that often require high temperature and/or high pressure [10–12]. Nevertheless, conducting such a reaction under aerobic conditions usually leads to the production of various kinds of reactive oxygen species (ROS), due to the simultaneous oxidation of H_2O and reduction of O_2 , leading to insufficient or excessive oxidation of catalytic substrates [13,14]. To overcome these challenges, sacrificial reagents in the form of electron donors or acceptors have been

widely employed in photocatalytic redox systems [14,15]. Unfortunately, the use of sacrificial reagents wastes half of the solar energy and may produce hard-to-separate byproducts [16]. A win-win strategy involves integrating photocatalytic CO_2 reduction with organic oxidation into one photoredox reaction system. By doing so, the organic substrates can directly replace sacrificial agents to trap photogenerated holes under anaerobic conditions, which avoids the consumption of photo-generated electrons by O_2 and promotes the overall efficiency of the system [17,18]. Recently, several attempts have been made to couple photocatalytic CO_2 reduction with alcohol oxidation [19,20]. However, the oxidation of saturated C-H bonds poses a formidable challenge due to the higher bond energy and lower selectivity [10,13]. Therefore, the development of novel photocatalysts for coupled photoredox reactions, capable of both CO_2 reduction and C-H oxidation (i.e., toluene oxidation), is of great importance in the realm of photocatalysis and organic synthesis.

To simultaneously achieve CO_2 reduction and toluene oxidation, the

* Corresponding author.

** Corresponding author at: Key Laboratory of the Ministry of Education for Advanced Catalysis Materials, Zhejiang Normal University, Jinhua, Zhejiang 321004 China.

E-mail addresses: ahmed503@zjnu.edu.cn (A.M. Idris), zqli@zjnu.edu.cn (Z. Li).

photocatalyst must possess sufficiently negative conduction band (CB) and positive valence band (VB) potentials that meet the required thermodynamic potentials and kinetic overpotentials [10,21]. Such strict criteria are difficult to fulfill by a single visible-light response photocatalyst [22,23]. Constructing heterojunctions composed of two visible-light responsive photocatalysts offers a promising solution. Among various heterojunctions, type II and S-scheme are regarded as two efficient systems for spatial charge separation and facilitating two redox half-reactions [23–25]. However, in a type II heterojunction, the charge flow tends to keep the photogenerated charges with lower redox potentials, limiting their capability to drive two simultaneous redox half-reactions [22,26]. In contrast, an S-scheme heterojunction retains higher energy electrons and holes while preserving strong redox capability at two different semiconductors, meeting the requirements for simultaneous redox reductions [24,27]. Therefore, rationally designing an S-scheme heterojunction with suitable component semiconductors is crucial for driving a coupled photoredox system. Of note, the S-scheme concept has properly addressed the weaknesses in traditional liquid and all-solid-state Z-scheme mechanisms. It incorporates factors such as work function, Fermi level alignment, internal electric field (IEF), and band bending, in addition to staggered band alignment [24,28].

Metal halide perovskites, such as CsPbBr_3 nanocrystals (CPB NCs), have gained significant attention as a distinct reductive visible light responsive photocatalyst for reduction reactions due to their suitable bandgap, sufficient reduction potential, and abundant surface sites [29, 30]. In contrast, metal oxide semiconductors responsive to visible light with adequate oxidation potential are highly desirable for oxidation reactions [11,31,32]. For example, $\text{W}_{18}\text{O}_{49}$, especially in the form of ultrathin nanowires (UTNWs), has emerged as a promising and stable oxidative photocatalyst due to its unique structure and composition, which provides a large surface area, distinct electronic configuration, and adequate active sites, all of which contribute to enhanced photocatalytic oxidation performance [33–35]. Hence, constructing an S-schemed heterojunction with a high-quality interface based on CPB NCs and $\text{W}_{18}\text{O}_{49}$ UTNWs is highly desirable for enhancing charge separation and providing active sites for two coupled photoredox reactions in one photocatalytic system.

Demonstrated herein is a meticulous high-quality interface S-scheme heterostructure of $\text{W}_{18}\text{O}_{49}/\text{CsPbBr}_3$ (labeled as WOCPB) via an *in-situ* hot injection growth method towards enhanced a coupled bifunctional photoredox system involving photocatalytic reduction of CO_2 to CO and selectively oxidizing toluene to benzaldehyde (BD). Detailed morphological investigations unravel that the resulting WOCPB heterojunction exhibits distinctive morphology, with the CPB NCs growing effectively along the surface of the bundle-like $\text{W}_{18}\text{O}_{49}$ UTNWs. Comprehensive experimental results combined with density functional theory (DFT) simulations disclose that the IEF was established upon forming WOCPB heterojunction due to the staggered Fermi level and band alignment. This configuration reveals a valid S-scheme pathway for photogenerated charge carriers. Benefiting from the advantageous straddling redox potential and spatial charge separation brought by S-scheme configuration, the developed WOCPB heterojunction realizes decent bifunctional photocatalytic activities of CO_2 -to-CO conversion ($143 \mu\text{mol g}^{-1} \text{h}^{-1}$) and selective oxidation of toluene to BD ($1546 \mu\text{mol g}^{-1} \text{h}^{-1}$) under visible light irradiation.

2. Experimental section

2.1. Synthesis of $\text{W}_{18}\text{O}_{49}$ UTNWs

The $\text{W}_{18}\text{O}_{49}$ UTNWs were synthesized by heating $\text{W}_{18}\text{O}_{49}$ nanowires (NWs) in an organic solvent. Initially, the $\text{W}_{18}\text{O}_{49}$ NWs were synthesized using a solvothermal method as described in the previous report [34]. In a typical synthesis of $\text{W}_{18}\text{O}_{49}$, 43 mg of WCl_6 was dissolved in 30 mL of anhydrous ethanol and stirred for 30 min. Subsequently, the mixture was transferred into a 50 mL Teflon-lined autoclave, which was sealed

inside a stainless-steel autoclave and heated at 200 °C for 12 h. The resulting $\text{W}_{18}\text{O}_{49}$ NWs were collected and washed with ethanol several times and dried in a vacuum at 60 °C overnight. Subsequently, the obtained $\text{W}_{18}\text{O}_{49}$ NWs were used as a precursor for the preparation of $\text{W}_{18}\text{O}_{49}$ UTNWs. In this process, the prepared $\text{W}_{18}\text{O}_{49}$ NWs were dispersed in 10 mL of organic solvent octadecene (ODE) containing 1 mL of oleic acid (OA) and 2 mL of oleylamine (OAm), and heated to 100 °C for 10 min to yield blue flocculent $\text{W}_{18}\text{O}_{49}$ UTNWs.

2.2. Synthesis of WOCPB heterojunction

WOCPB heterojunction was prepared by *in-situ* growth of CPB NCs on the $\text{W}_{18}\text{O}_{49}$ UTNWs. In a typical procedure, 300 mg of the freshly prepared $\text{W}_{18}\text{O}_{49}$ UTNWs along with 0.207 g of PbBr_2 and 12 mL of ODE, were added into a 25 mL three-necked flask. The flask system was continuously magnetically stirred under the Ar flow, and heated to 120 °C for 30 min. Meanwhile, a solution containing 0.215 g of Cs_2CO_3 in 10 mL of ODE and 1.5 mL of OA was prepared at 150 °C under Ar protection to obtain the stock solution of Cs-OA. Subsequently, 3 mL of OA and 1.65 mL of OAm were added to the PbBr_2 precursor. Then, the solution was heated at 145 °C until the PbBr_2 was fully dissolved. After that 1.2 mL of Cs-OA stock solution was injected swiftly. After 5 s of reaction, the mixture was cooled to room temperature using an ice-water bath. The resulting solid WOCPB heterojunction was washed with 5 mL of ethyl acetate (EA) and dried at 40 °C for 6 h under vacuum. The control sample of WOCPB-NWs (thick $\text{W}_{18}\text{O}_{49}$ NWs/CPB heterojunction) was also prepared using the same method as WOCPB heterojunction, with the only difference being that the precursor was replaced with the $\text{W}_{18}\text{O}_{49}$ NWs. As for the pure CPB NCs, they were synthesized using the same method as described above, except without the use of the $\text{W}_{18}\text{O}_{49}$ UTNWs precursor.

3. Results and discussion

The WOCPB heterojunction was prepared by the *in-situ* growing of CPB NCs on $\text{W}_{18}\text{O}_{49}$ UTNWs using the hot-injection method, as illustrated schematically in Fig. 1a (for details, see experimental section). The transmission electron microscopy (TEM) image in Fig. S1a shows that the as-prepared $\text{W}_{18}\text{O}_{49}$ consists of regular NWs with a thickness ranging from 20 to 50 nm and lengths extending to micrometers. In contrast, the TEM in Fig. 1b and S2a indicate that after subjecting the $\text{W}_{18}\text{O}_{49}$ NWs to a heating treatment in ODE with long-chain ligands, bundle-like $\text{W}_{18}\text{O}_{49}$ UTNWs with average ultrathin nanowires with diameter below 5 nm were observed. The bundle-like morphology may originate from the self-assembly of nanowires through Van der Waals interaction under the assistance of long-chain ligands in solution [36, 37]. Upon the *in-situ* growth of CPB NCs on $\text{W}_{18}\text{O}_{49}$ UTNWs to form the WOCPB heterojunction, particles of CPB NCs were found to envelop and align precisely along the surface of the $\text{W}_{18}\text{O}_{49}$ UTNWs (Fig. 1c and Fig. S3). Interestingly, within the WOCPB heterojunction, the morphology and lateral sizes of the CPB NCs (about 7 nm) remained consistent with the pristine CPB NCs (Fig. S4a), indicating that the CPB NCs do not undergo any Ostwald ripening, underscoring the delicate control achieved through the current *in-situ* synthetic approach.

Besides, the corresponding high-resolution transmission electron microscopy (HRTEM) analysis of the WOCPB heterojunction revealed the coexistence of highly crystalline CPB NCs with a lattice spacing fringe of 0.58 nm matching the (100) plane and $\text{W}_{18}\text{O}_{49}$ UTNWs with a lattice spacing fringe of 0.38 nm corresponding to the (010) plane (Fig. 1d). This observation suggests that both CPB NCs and $\text{W}_{18}\text{O}_{49}$ UTNWs are in high crystallinities. Figs. 1e-1j show the analysis of energy-dispersive X-ray spectroscopy (EDX) elemental mapping, manifesting the existence of the W, O, Cs, Pb, and Br elements in the WOCPB heterojunction, which is aligned with the results from the full X-ray survey spectra (Fig. S5). All the aforementioned results confirm the successful formation of the WOCPB heterostructure with solid

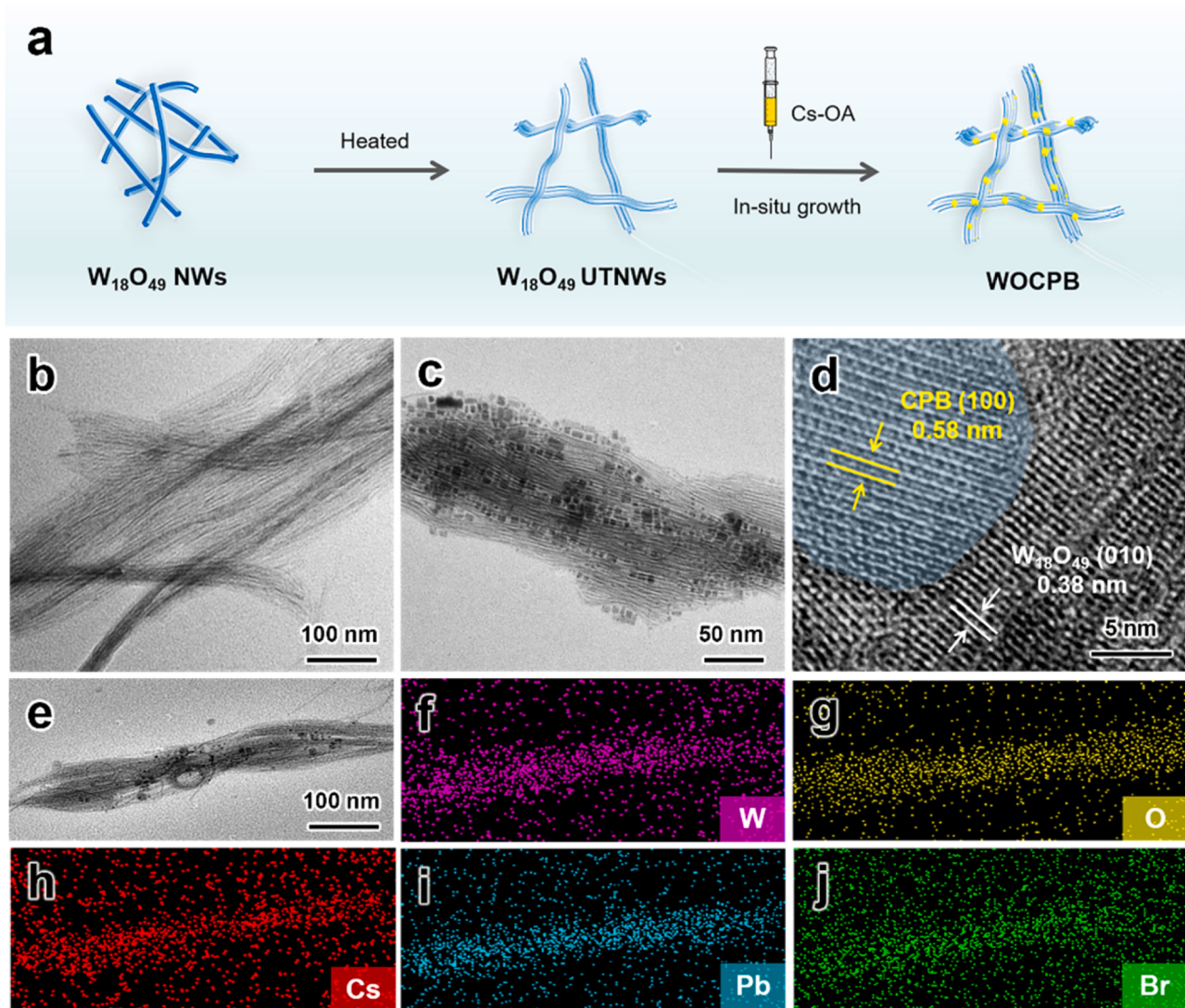


Fig. 1. (a) Schematic illustration for preparing WOCPB heterojunction. TEM images of (b) W₁₈O₄₉ UTNWs and (c) WOCPB. (d) HRTEM image of WOCPB and (e-j) corresponding elemental mapping for W, O, Cs, Pb, and Br.

interaction between W₁₈O₄₉ UTNWs and CPB NCs.

The phase purity and crystallinity of the prepared samples were verified by powder X-ray diffraction pattern (XRD). Both W₁₈O₄₉ NWs and W₁₈O₄₉ UTNWs collaborate well with monoclinic W₁₈O₄₉ (JCPDS No. 71-2450 (Figs. S1b and S2b)) [33,34]. Fig. S4b shows that CPB NCs accorded well with the cubic phase of cesium lead halide (JCPDS No. 54-0752) [38,39]. Notably, the diffraction peaks of the W₁₈O₄₉ UTNWs and CPB NCs in the WOCPB heterojunction are well indexed with their standard XRD patterns without any impurities, implying the *in-situ* growth method does not alter the respective crystal structures of WOCPB heterojunction (Fig. S6). UV-visible diffuse reflectance spectra (DRS) were utilized to elucidate the optical properties of the prepared samples [40,41]. Figs. 2a and 2b indicate that the absorption spectra of the W₁₈O₄₉ UTNWs and CPB NCs correspond to bandgaps of 2.81 and 2.29 eV, respectively (inset Figs. 2a and 2b). The work functions (Φ) of W₁₈O₄₉ UTNWs and CPB NCs were determined by ultraviolet photoelectron spectroscopy (UPS) [42,43]. By subtracting the cutoff binding energy (E_{cutoff}) from the excitation energy ($h\nu = 21.2$ eV), their absolute values were calculated to be approximately 4.73 eV and 4.23 eV ($h\nu - E_{\text{cutoff}}$), respectively (Fig. 2c). Accordingly, the VB positions for W₁₈O₄₉ and CPB are around 2.66 and 2.01 eV vs. Fermi level (E_F), respectively (Fig. 2d). Therefore, after calibrating the vacuum level to

reversible hydrogen level (4.44 eV for 0 V), the VB maximum (VBM) position of W₁₈O₄₉ and CPB are around *ca.* 2.95 V and 1.80 V (vs. RHE), respectively. Using the $E_{\text{CB}} = E_{\text{VB}} - E_g$ equation, the CB minima (CBMs) of the W₁₈O₄₉ UTNWs and CPB NCs were calculated to be 0.14 V and *–*0.49 V (vs. RHE), respectively. Based on the above calculations, the VB and CB of the W₁₈O₄₉ UTNWs and CPB NCs were schematically depicted in Fig. 2e.

3.1. Charge transfer direction mechanism

It is widely recognized that the shifts in binding energies (BEs) of the elements that stem from changes in valence states or electron density within heterostructure photocatalysts can effectively indicate the electron transfer direction in the heterojunction [27,44]. Generally, if the element gains an electron, its BE decreases. Analogously, if the element loses an electron, its BE increases [45]. To probe the charge transfer direction in the WOCPB heterojunction, a comparative study of the X-ray photoelectron spectroscopy (XPS) spectra of pure W₁₈O₄₉, CPB, and the WOCPB heterojunction (see Fig. 3a-d) was conducted. In comparison with CPB, the BEs of Cs 3d, Pb 4f, and Br 3d in WOCPB heterojunction positively shift in the dark, indicating a decrease in the electron density of CPB. In contrast, when compared with W₁₈O₄₉, the

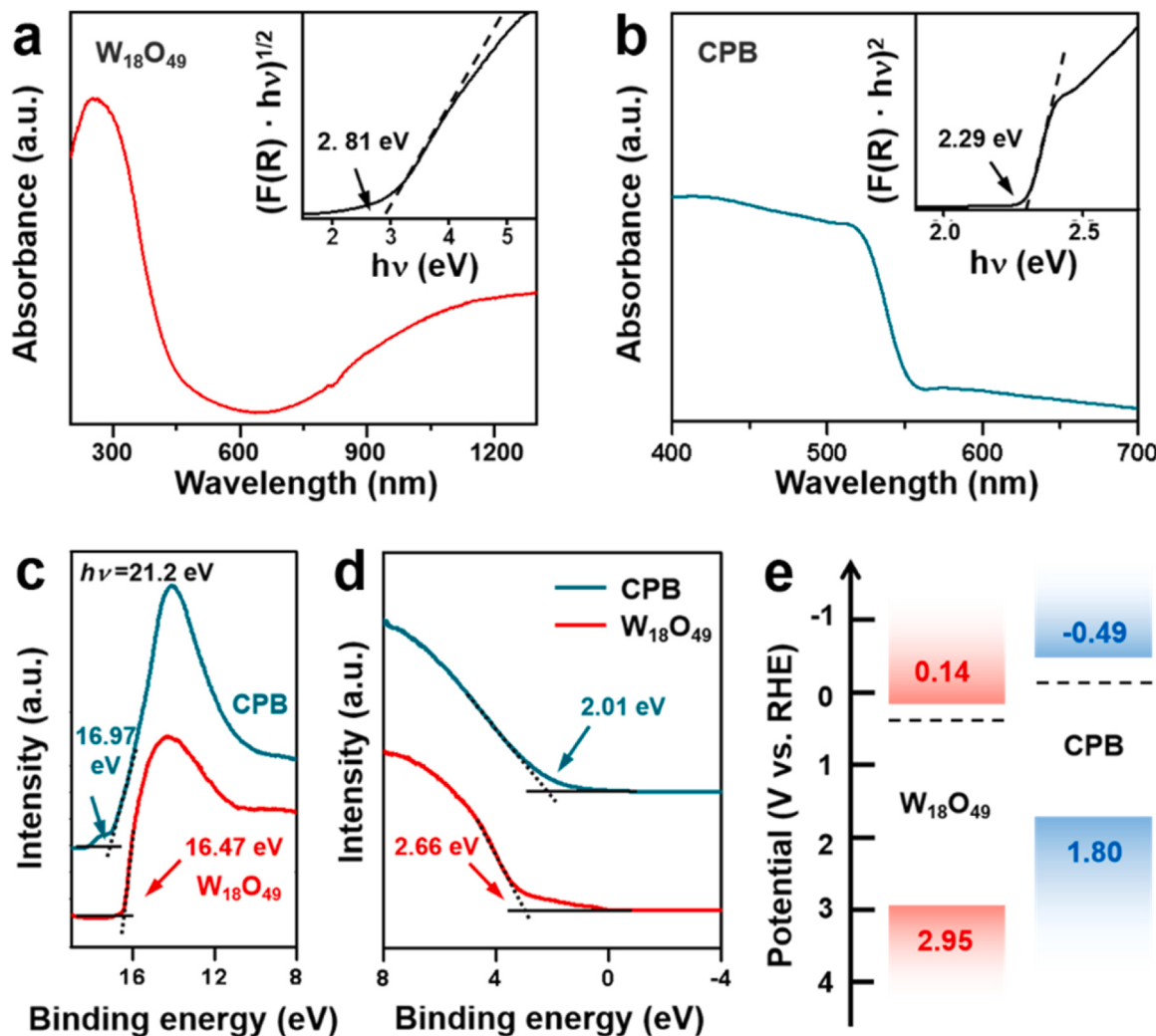


Fig. 2. (a, b) UV-vis DRS spectra and bandgap energy (insets) of the $\text{W}_{18}\text{O}_{49}$ UTNWs and CPB NCs display their corresponding bandgaps. (c) UPS measurements of work functions and (d) VB positions of samples obtained by the VB spectra and secondary electron cutoff (E_{cutoff}). (e) Corresponding staggered band alignment of $\text{W}_{18}\text{O}_{49}$ UTNWs and CPB NCs.

binding energy of W 4 f in the WOCPB heterojunction negatively shifts in the dark, implying a charge transfer from CPB to $\text{W}_{18}\text{O}_{49}$ upon their contact. Moreover, the *in-situ* light irradiation XPS spectra of the Cs 3d and Pb 4 f in the WOCPB heterojunction showed significant negative shifts by 0.2 eV and 0.35 eV, respectively, compared with WOCPB in darkness. In contrast, the Br 3d exhibited a slight shift of about 0.15 eV. These results suggested the accumulation of the photogenerated electrons at the CPB side. Similarly, the BE of W 4 f in the WOCPB heterojunction under light irradiation exhibited a slight positive shift (0.1 eV) compared to those in darkness, indicating a reduction of electrons cloud density near the W atom in the $\text{W}_{18}\text{O}_{49}$ UTNWs. These results suggested that under light irradiation, the photogenerated electrons transfer from the CBM of $\text{W}_{18}\text{O}_{49}$ UTNWs to the VBM of CPB NCs across the WOCPB heterojunction interface *via* an S-scheme mechanism.

To reinforce the aforementioned conclusion, electron paramagnetic resonance (EPR) was conducted to explore the charge transfer mechanism in the WOCPB heterojunction. 5,5-dimethyl-1-pyrroline N-oxide (DMPO) was employed as superoxide radical ($\bullet\text{O}_2$) and hydroxyl radical ($\bullet\text{OH}$) trapping agent [25,46,47]. The EPR results in Fig. 3e indicate that four peaks corresponding to the DMPO- $\bullet\text{O}_2$ signals were observed for the pristine CPB NCs and WOCPB heterojunction under light irradiation. However, no DMPO- $\bullet\text{O}_2$ signal peaks were recorded for the pristine $\text{W}_{18}\text{O}_{49}$ UTNWs due to their high oxidation nature and positive reduction potential. In contrast, Fig. 3f shows that $\text{W}_{18}\text{O}_{49}$ UTNWs and

WOCPB heterojunction have signal peaks corresponding to the DMPO- $\bullet\text{OH}$, where no DMPO- $\bullet\text{OH}$ signal peaks were observed for the CPB due to its high reduction nature and limited oxidation potential. Interestingly, the WOCPB heterojunction displayed significantly higher DMPO- $\bullet\text{O}_2$ and DMPO- $\bullet\text{OH}$ intensity peaks compared to the pristine CPB NCs and $\text{W}_{18}\text{O}_{49}$ UTNWs counterparts, implying that within the WOCPB heterojunction, the photogenerated electrons are predominantly accumulated at the CPB side, while the photogenerated holes are primarily accumulated at the $\text{W}_{18}\text{O}_{49}$ UTNWs side. This result follows the result from the *in-situ* light irradiation XPS spectra.

To further affirm the aforementioned results, the work function and Fermi level of the CPB and $\text{W}_{18}\text{O}_{49}$ were also evaluated by DFT simulations. Figs. 4a and 4b illustrate that the theoretically calculated surface work function of the $\text{W}_{18}\text{O}_{49}$ (5.05 eV) is higher than that of the CPB (4.48 eV). Upon the formation of the WOCPB heterojunction, since the CPB has a lower work function and higher Fermi level compared to the $\text{W}_{18}\text{O}_{49}$ (Fig. 4c), it is thermodynamically favorable that the electrons will spontaneously migrate from the CPB side toward the $\text{W}_{18}\text{O}_{49}$ side until the alignment of the Fermi levels of two-components [28,40,48, 49]. Consequently, the electron depletion/accumulation layer would be established under the system's equilibrium. As such, the surface of the CPB becomes positively charged, while the surface of the $\text{W}_{18}\text{O}_{49}$ becomes negatively charged, giving rise to building a solid IEF and band binding from CPB to $\text{W}_{18}\text{O}_{49}$ (Fig. 4d). This configuration provides a

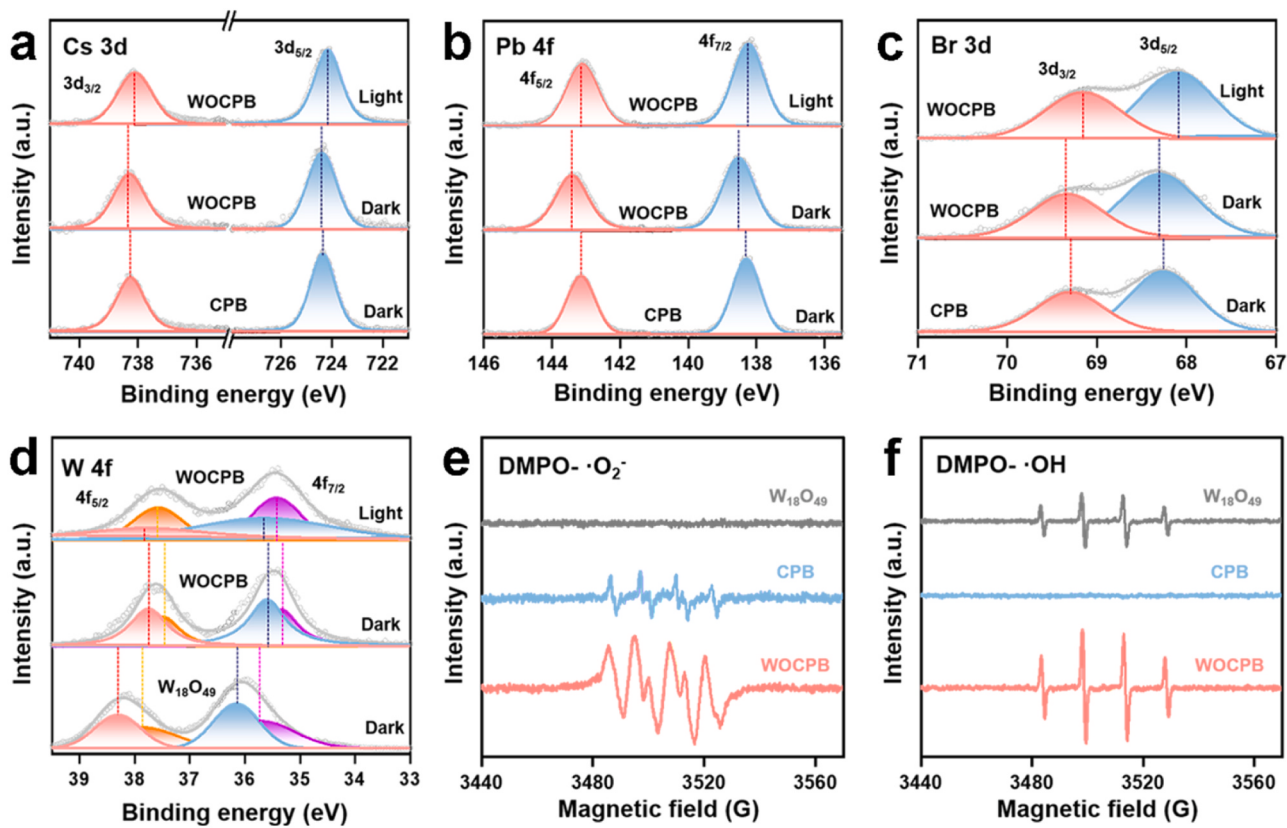


Fig. 3. High-resolution XPS spectra of (a) Cs 3d, (b) Pb 4 f, (c) Br 3d, and (d) W 4 f under different conditions (light vs. dark) depicted comparatively according to the constituent. EPR spectra of (e) DMPO-•O₂⁻ in a saturated O₂ acetonitrile solution and (f) DMPO-•OH in acetonitrile/water (volume ratio of 200:1) dispersion in the presence of W₁₈O₄₉ UTNWs, CPB NCs, and WOCPB heterojunction.

strong driving force for the charge transfer between heterojunctions. Under light irradiation, the IEF induces the photogenerated electrons in the CBM of the W₁₈O₄₉ to recombine with photogenerated holes in the VBM of the CPB following S-scheme electron transfer mode (Fig. 4e). As such, it allows the preservation of photogenerated electrons at the CBM of the CPB and photogenerated holes at the VBM of the W₁₈O₄₉. Thermodynamically, the estimated redox potentials of the WOCPB heterojunction are straddled to the theoretical potentials for simultaneously driving a reduction reaction at the CPB side and an oxidation reaction at the W₁₈O₄₉ side under visible light irradiation.

3.2. Assessment of bifunctional photocatalytic activity

To fully exploit the intriguing advantages of the WOCPB heterojunction brought by the S-scheme mechanism, a visible-light-driven photocatalytic redox reaction involving CO₂ reduction coupled with toluene oxidation was proposed without using any redox sacrificial reagents. As seen in Fig. 5a, the pristine W₁₈O₄₉ UTNWs only facilitate the oxidation half-reaction of toluene, resulting in a trace amount of BD, and no CO gas was observed due to the insufficient reduction potential of the W₁₈O₄₉ UTNWs for CO₂ reduction [21,50]. Conversely, the photocatalytic performance of the pristine CPB NCs resulted in the production of a small amount of CO gas with a negligible amount of BD as an oxidation product. Strikingly, the WOCPB heterojunction simultaneously yields a high CO production rate of 143 μmol g⁻¹ h⁻¹ and selective oxidation of toluene to BD with a production rate of 1546 μmol g⁻¹ h⁻¹ and selectivity of 80%, and benzyl alcohol (BA) as a byproduct with a production rate of 387 μmol g⁻¹ h⁻¹. Optimal results are achieved at the mass ratio of 6:1 for W₁₈O₄₉ UTNWs to CPB NCs (Fig. 5b). The time-dependent photocatalytic activity of the WOCPB heterojunction (five runs, each lasting 3 h) in Fig. 5c indicate a steady increase in the

production yields of CO and BD over the reaction time without any evident decay. These results underscore the high photostability of the developed WOCPB heterojunction. Moreover, the TEM image and XRD pattern of the WOCPB heterojunction after the recycling experiments (Fig. S7) indicated no morphology alterations or impurity peaks were observed. This observation further highlights the excellent photostability of the WOCPB heterojunction.

To validate the role of each component in the photoredox system over WOCPB heterojunction, a series of control experiments were conducted (Table S1). Entries 1 and 2 indicate that no photoactivity was detected without the WOCPB heterojunction and/or light irradiation, confirming the necessity of the WOCPB heterojunction and light irradiation for photoactivity [51]. When WOCPB heterojunction was exposed to air instead of CO₂ and toluene, only BD was formed (entry 3). Substituting acetonitrile/water (49:1, v: v) for toluene in the presence of WOCPB heterojunction and CO₂, only CO gas was detected because acetonitrile may act as a hole-accepting sacrificial reagent (in entry 4) [52]. Control experiments and isotope labeling techniques suggest that the CO product indeed originated from the photocatalytic reduction of CO₂ (as shown in Fig. S8). Besides, the experiments for active species trapping were also carried out to trace the origin sources of the products [53,54]. When potassium persulfate (K₂S₂O₈) was used as an electron-trapping reagent [11,55], only a decent production rate of BD was detected (entry 5). On the contrary, when ammonium oxalate (NH₄C₂O₄) was added as a hole-trapping reagent [11,32], only CO and a trace amount of BD were detected (entry 6). The results from entries 5 and 6 confirm that the photogenerated electrons and holes are the main active species for simultaneously producing CO and BD over WOCPB heterojunction (entry 9). Additionally, the utilization of tert-butyl alcohol (TBA) as a scavenger for •OH resulted in a significant inhibition in the photocatalytic oxidation reaction (entry 7). Analogously,

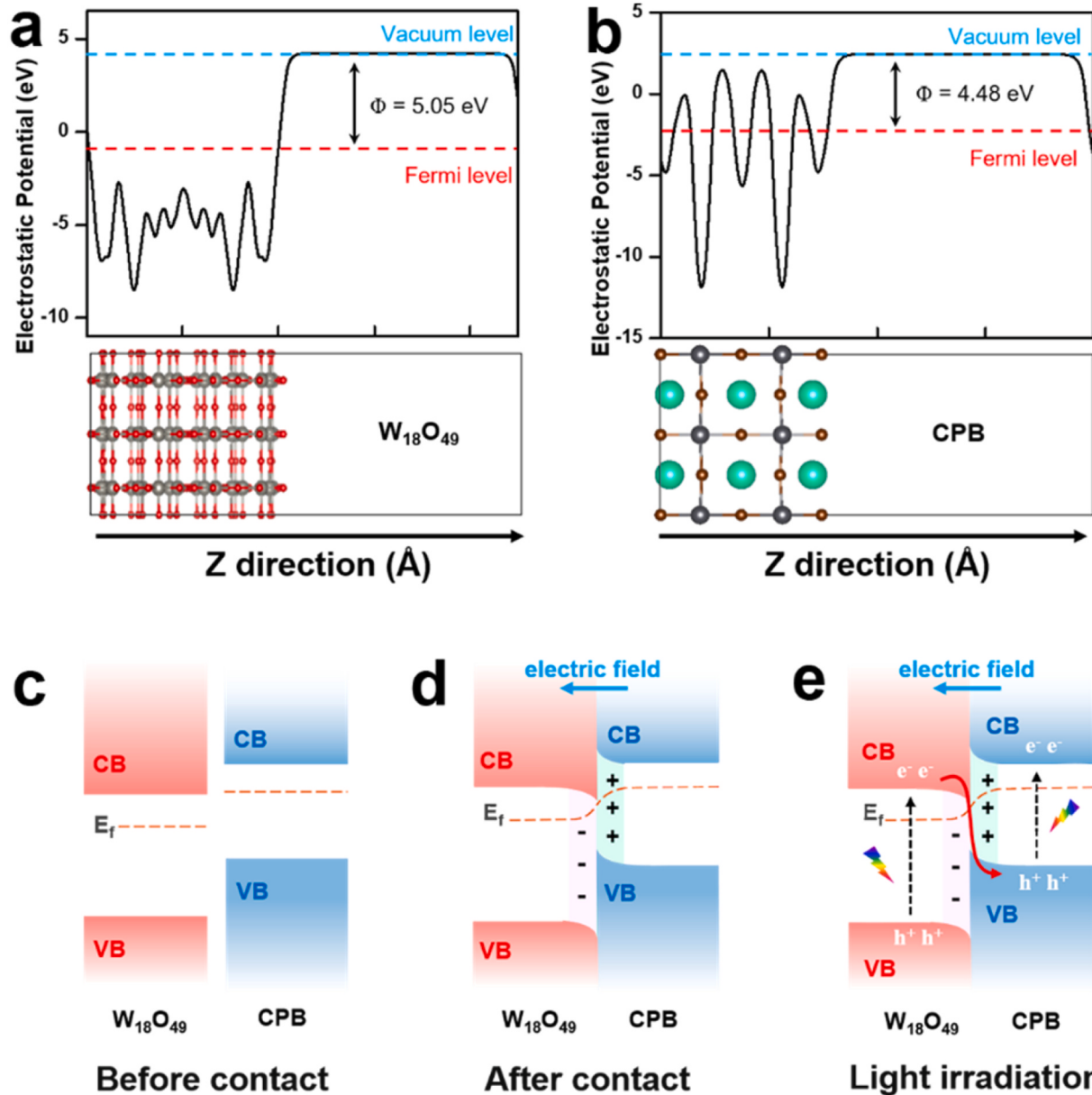


Fig. 4. The calculated work functions and corresponding structural models of (a) $W_{18}O_{49}$ (010) surface, and (b) CsBr-terminated CPB (001) surface. Color code; dark grey, Pb; brown, Br; cyan, Cs; grey, W; and red, O. Illustration of band structures between $W_{18}O_{49}$ and CPB (c) before contact, (d) contact in the dark, and (e) under light irradiation. The E_f bending at the interface was considered in (d) and (e).

when p-benzoquinone (p-BQ) was employed as a scavenger for $\cdot O_2^-$, no noticeable inhibition was observed in both oxidation and reduction reactions (entry 8). These results indicate that photogenerated holes play a crucial role in the activation of toluene molecules, and the resulting carbon-center radical is more easily oxidized by the $\cdot OH$. All aforementioned results strongly supported that the enhanced simultaneous photocatalytic reduction of CO_2 to CO and selective oxidation of toluene to BD in the coupled photoredox system indeed originated from fully utilizing the advantages of spatial charge separation and high redox potential of the WOCPB heterojunction.

To speculate the reaction mechanism and the adsorbed intermediates during the photocatalytic redox reactions, the time-dependent *in situ* diffuse reflectance infrared Fourier-transform spectroscopy (DRIFTS) was carried out [56–58]. As illustrated in Fig. 5d, the typical absorption peak at 1613 cm^{-1} was observed when the WOCPB heterojunction was exposed to a mixture of CO_2 and toluene, attributing to the $CO_2^\delta^-$ species [59]. Typical characteristic bands of toluene such as the C-H stretching

vibration of aromatic ring (3076 and 3038 cm^{-1}) and methyl group (2943 and 2882 cm^{-1}) can also be observed [60]. In contrast, when the WOCPB heterojunction was exposed to a mix of CO_2 and toluene under light irradiation, typical intermediate absorption peaks corresponding to *COOH (1557 cm^{-1}), monodentate carbonate ($m-CO_3^{2-}$) groups (1543 , 1513 , and 1458 cm^{-1}), and *CO species (2078 cm^{-1}) were observed [57,59,61,62]. Besides, typical intermediate absorption peaks located at 1697 cm^{-1} (light-blue marked region) and 1212 cm^{-1} (highlighted in light blue) correspond to the stretching vibration of the carbonyl group ($C=O$) of BD, and the stretching vibration of $C-O$ in BA, respectively, were detected [60].

Moreover, a typical absorption peak at 1645 cm^{-1} corresponding to the bending vibration of water (δ_{H_2O}) was observed [63], confirming the formation of H_2O in the reaction pathway of CO_2 reduction. Interestingly, all peak intensities significantly increased with increasing irradiation time from 0 to 60 minutes. Notably, the results in Figs. S9 and S10 indicate that the variation in peak intensity in WOCPB

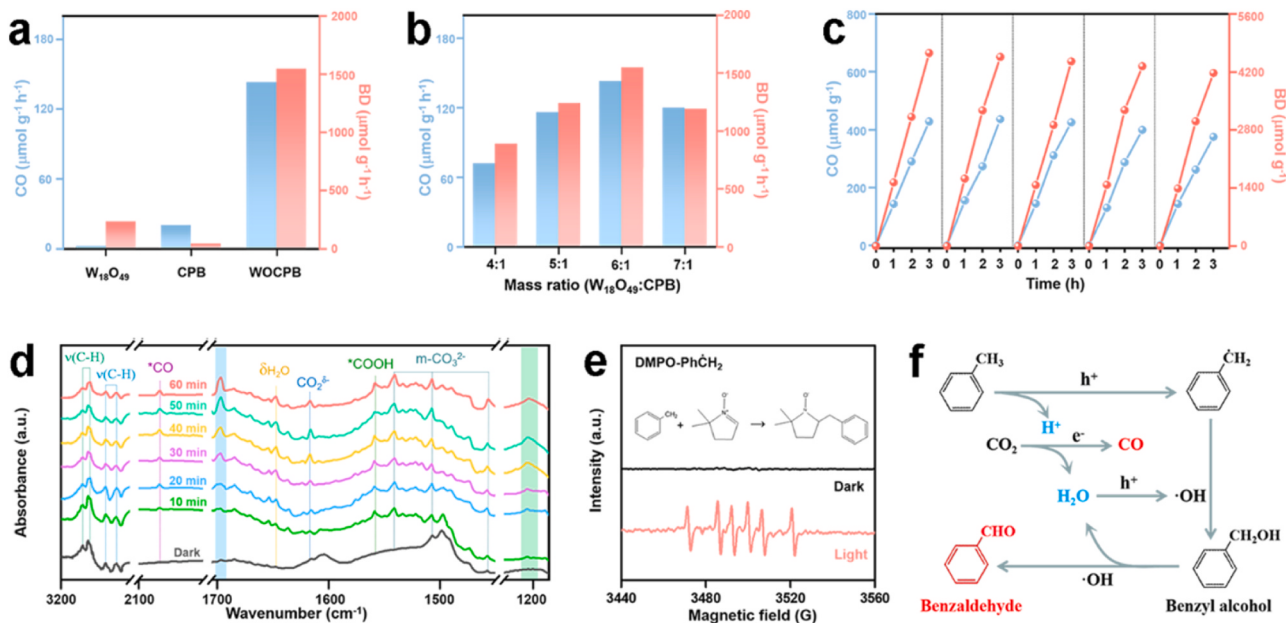


Fig. 5. Photocatalytic reduction of CO₂ and oxidation of toluene over (a) pure W₁₈O₄₉ UTNWs, pure CPB NCs, and WOCPB heterojunction; (b) WOCPB heterojunctions prepared with different mass ratios between W₁₈O₄₉ UTNWs and CPB NCs; (c) Corresponding stability test of WOCPB heterojunction. (d) *In-situ* DRIFT spectra of WOCPB heterojunction with a mixture of CO₂ and toluene under visible light illumination. (e) *In-situ* EPR spectra for identifying the monitor C_α radicals in a saturated CO₂ toluene solution over the WOCPB heterojunction under dark and light irradiation. (f) Schematic illustration of the photocatalytic mechanism for bifunctional photocatalytic reaction in WOCPB heterojunction.

heterojunction during the photocatalytic reaction is significantly higher compared to other reduction or oxidation half-reactions, meaning a more pronounced driving force for the photoredox reaction facilitated by synergistic photocatalytic systems. To gain deeper insight into the reaction pathway of the developed system, an *in-situ* EPR was conducted. As shown in Fig. 5e, under light irradiation, the WOCPB heterojunction exhibits six characteristic signal peaks, corresponding to the generation of the intermediate C_α radicals [64,65], and no signal of DMPO-•CH₂Ph radicals was observed in the dark. This suggests that photogenerated holes on the VB of W₁₈O₄₉ oxidize toluene under light irradiation, forming H⁺ and benzyl radicals. Whereas, the photogenerated electrons on the CB of CPB can interact with H⁺ and reduce CO₂ to form CO and H₂O (CO₂ + 2 H⁺ + 2 e⁻ → CO + H₂O) [66–68]; meanwhile, the holes oxidize water into •OH radicals and further oxidize the benzyl radical to produce the BD and BA products.

Based on the above results, a plausible reaction process of photocatalytic CO₂ reduction coupled with toluene selective oxidation over the WOCPB heterojunction was schematically proposed in Fig. 5f. (1) Under the light irradiation, the photogenerated electrons and holes are separated and transferred to the surfaces of CPB and W₁₈O₄₉, respectively, engaging in photocatalytic reactions. (2) The highly oxidative photogenerated holes initially oxidize the C-H bond of toluene, generating •CH₂Ph and protons. Simultaneously, CO₂ molecules and protons from toluene react with the photogenerated electrons, forming water and CO, respectively. (3) Subsequently, the photogenerated holes oxidize H₂O to form •OH radicals to serve as active species for further oxidation of the carbon-centered benzyl group. (4) Ultimately, the carbon-centered benzyl radicals react with •OH to produce BA and subsequent BD products.

3.3. Investigation of charge carrier kinetics

To elucidate the enhanced simultaneous photoredox reactions of the WOCPB heterojunction, the charge carrier kinetics were experimentally investigated by photoelectrochemical techniques. As displayed by the transient photocurrent result in Fig. 6a, the WOCPB heterojunction exhibits a stable, positive, and 4-fold intense photocurrent density

compared to pristine CPB NCs and W₁₈O₄₉ UTNWs. This result verifies the effective separation of photogenerated charges over WOCPB heterojunction. Likewise, electrochemical impedance spectroscopy (EIS) demonstrated a Nyquist plot where the WOCPB heterojunction exhibited smallest arc radius, manifesting that the heterojunction faced lower charge transfer resistance, benefiting fast separation and transfer of photogenerated charges (Fig. 6b). Moreover, steady-state photoluminescence (PL) spectra in Fig. 6c show that the PL spectrum of pristine CPB NCs is significantly quenched after the formation of the WOCPB heterostructure. The corresponding time-resolved PL spectra analysis in Fig. 6d, Table S2, demonstrates that the average emission lifetime (τ_{avg}) remarkably reduces from 12.96 ns for pristine CPB NCs to 5.91 ns for the WOCPB heterojunction. The steady-state and corresponding time-resolved PL spectra suggest that the charge transfer in the WOCPB heterojunction is a nonradiative quenching pathway. Hence, all the above kinetics characterizations manifested that the construction of the WOCPB heterojunction between CPB NCs and W₁₈O₄₉ UTNWs enhances spatial charge separation.

It is essential to highlight here that controlling the morphology, dimensions, and size of semiconductor photocatalysts plays a crucial role in influencing their physicochemical features [65,69]. To explore the impact of morphology and dimensional controlling on photocatalytic redox reactions, a comparative study was conducted between two types of heterojunctions: one prepared by W₁₈O₄₉ UTNWs and another prepared with thick W₁₈O₄₉ NWs (labeled as WOCPB-NWs heterojunction). Compared to the WOCPB heterojunction, the WOCPB-NWs heterojunction exhibits lower photocatalytic activity, lower photocurrent, larger arc radius, and stronger PL emission (Figs. S11 and S12). One possible reason behind the inferior photocatalytic activities of the WOCPB-NWs heterojunction is presumably due to the ultrahigh length-to-diameter of the W₁₈O₄₉ UTNWs compared to that of the W₁₈O₄₉ NWs. Moreover, semiconductor photocatalysts generally benefit from high specific surface areas, which are critical for improving photocatalytic performance [70,71]. The W₁₈O₄₉ UTNWs demonstrate a larger surface area than the W₁₈O₄₉ NWs (Fig. S13). Additionally, the poor interfacial quality between the W₁₈O₄₉ NWs and the CPB NCs (see Fig. S14) leads to inferior charge transfer and severe charge

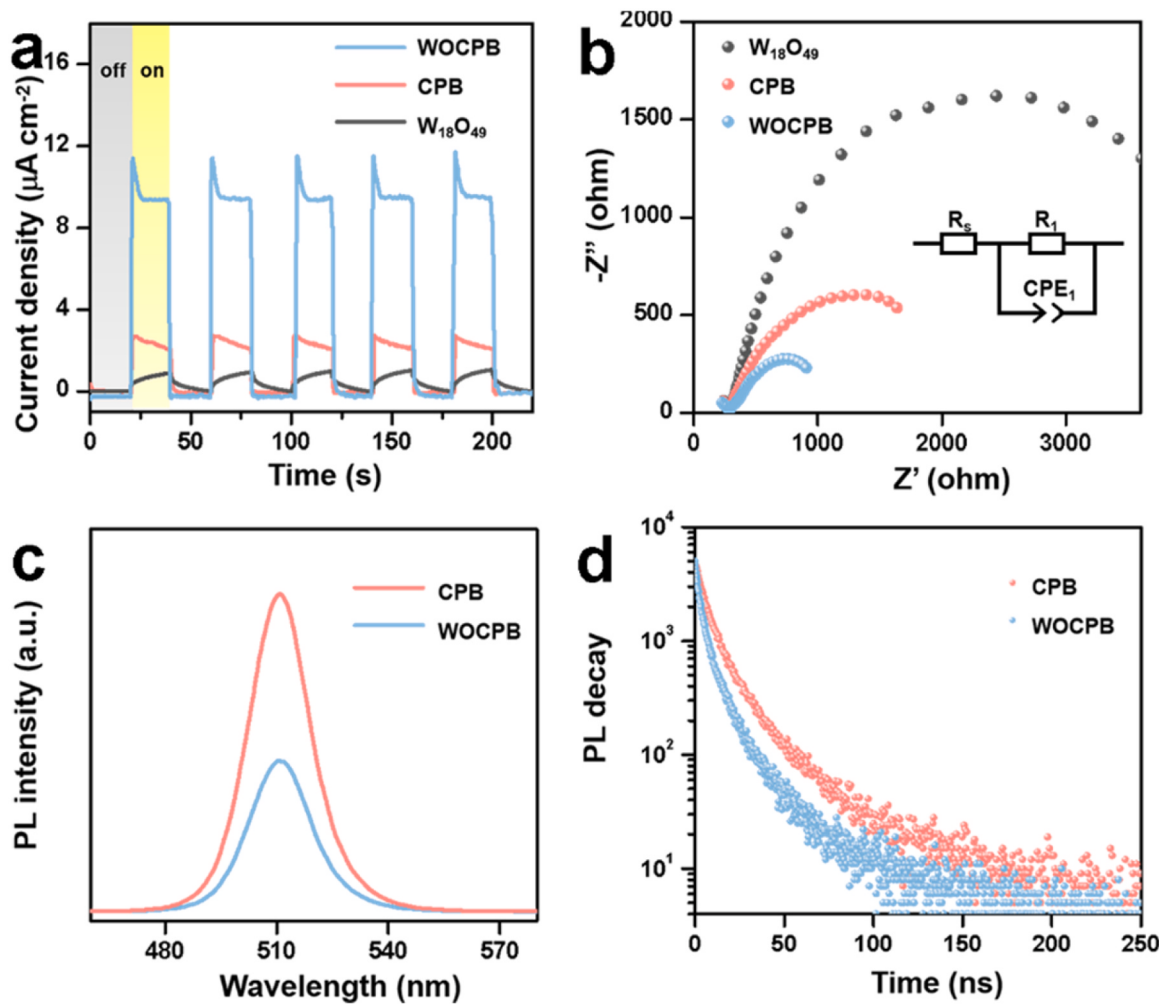


Fig. 6. Charge separation status of samples measured by different techniques: (a) photocurrents; (b) EIS (inset: the equivalent circuit, in the equivalent circuit, R_s , R_1 and CPE represent the series resistance, interface charge-transfer resistance, and constant phase element, respectively); (c) PL emission spectra ($\lambda_{\text{ex}} = 370$ nm); (d) TRPL ($\lambda_{\text{ex}} = 370$ nm; $\lambda_{\text{em}} = 513$ nm).

recombination. During the *in-situ* growing of CPB NCs, the formed CPB nuclei preferentially wrap and grow well along the surface of the $\text{W}_{18}\text{O}_{49}$ UTNWs. In contrast, growing the CPB NCs on $\text{W}_{18}\text{O}_{49}$ NWs with a tight interface is more challenging due to their smooth surface and smaller contact area. Consequently, in the WOCPB heterojunction with the $\text{W}_{18}\text{O}_{49}$ UTNWs, the interfacial interaction between $\text{W}_{18}\text{O}_{49}$ UTNWs and CPB NCs is more intimate than that in the WOCPB-NWs heterojunction. It is worth highlighting that several simultaneous bifunctional photo-redox systems have been reported recently, as shown in Table S3. However, to our knowledge, research demonstrating decent performance, simultaneously yielding high production of CO and selective oxidizing toluene to BD with an 80% selectivity is still rarely reported.

4. Conclusion

In summary, an intriguing WOCPB heterojunction S-scheme photocatalyst was fabricated *via* a facile *in-situ* growing approach to enhance visible-light-driven bifunctional photocatalysis involving CO_2 reduction coupled with toluene oxidation in a single photoredox system. Experimental characterizations integrated with DFT simulations reveal that the charge transfer direction in the WOCPB heterojunction follows the S-scheme charge transfer mode. Encouraging by the intriguing advantages of strong redox potentials and spatial charge separation of the WOCPB heterojunction, bifunctional photoredox reactions were studied in a mixed solution containing CO_2 and toluene as reactants. As a proof of

concept, remarkable photocatalytic yields were simultaneously achieved, resulting in a high CO production rate of $143 \mu\text{mol g}^{-1} \text{h}^{-1}$ and BD production rate of $1546 \mu\text{mol g}^{-1} \text{h}^{-1}$ with an 80% selectivity. This work sheds light on the rational design of multifunctional photocatalysts, offering a promising approach to maximize the utilization of the photogenerated carriers in synergetic photocatalytic systems.

CRediT authorship contribution statement

Li Zhengquan: Conceptualization, Funding acquisition, Investigation, Supervision, Writing – review & editing. **Wang Jin:** Supervision. **Peng Baojin:** Methodology. **Li Sheng:** Methodology. **Idris Ahmed Mahmoud:** Conceptualization, Supervision, Writing – original draft. **Shu Yang:** Investigation. **Chen Zhihao:** Formal analysis. **Jiang Xinyan:** Investigation, Visualization, Writing – original draft.

Declaration of Competing Interest

The authors declare that they have no known competing financial interests or personal relationships that could have appeared to influence the work reported in this paper.

Data Availability

Data will be made available on request.

Acknowledgments

This work was financially supported by the National Natural Science Foundation of China (21975223, 21701143) and the Natural Science Foundation of Zhejiang Province (LZ22B030002). Industrial Key Projects of Jinhua City (2021A22383).

Appendix A. Supporting information

Supplementary data associated with this article can be found in the online version at [doi:10.1016/j.apcatb.2024.123840](https://doi.org/10.1016/j.apcatb.2024.123840).

References

- [1] T. Inoue, A. Fujishima, S. Konishi, K. Honda, Photoelectrocatalytic reduction of carbon-dioxide in aqueous suspensions of semiconductor powders, *Nature* 277 (1979) 637–638, <https://doi.org/10.1038/277637a0>.
- [2] Y. Shen, C. Ren, L. Zheng, X. Xu, R. Long, W. Zhang, Y. Yang, Y. Zhang, Y. Yao, H. Chi, J. Wang, Q. Shen, Y. Xiong, Z. Zou, Y. Zhou, Room-temperature photosynthesis of propane from CO_2 with Cu single atoms on vacancy-rich TiO_2 , *Nat. Commun.* 14 (2023) 1117, <https://doi.org/10.1038/s41467-023-36778-5>.
- [3] X. Jiao, K. Zheng, Q. Chen, X. Li, Y. Li, W. Shao, J. Xu, J. Zhu, Y. Pan, Y. Sun, Y. Xie, Photocatalytic conversion of waste plastics into C_2 fuels under simulated natural environment conditions, *Angew. Chem. Int. Ed.* 59 (2020) 15497–15501, <https://doi.org/10.1002/ange.201915766>.
- [4] Y. Shi, Y. Zhou, Y. Lou, Z. Chen, H. Xiong, Y. Zhu, Homogeneity of supported single-atom active sites boosting the selective catalytic transformations, *Adv. Sci.* 9 (2022) 2201520, <https://doi.org/10.1002/advs.202201520>.
- [5] X. Xiong, C. Mao, Z. Yang, Q. Zhang, G.I.N. Waterhouse, L. Gu, T. Zhang, Photocatalytic CO_2 reduction to CO over Ni single atoms supported on defect-rich zirconia, *Adv. Energy Mater.* 10 (2020) 2002928, <https://doi.org/10.1002/aenm.202002928>.
- [6] W. Kim, B.A. McClure, E. Edri, H. Frei, Coupling carbon dioxide reduction with water oxidation in nanoscale photocatalytic assemblies, *Chem. Soc. Rev.* 45 (2016) 3221–3243, <https://doi.org/10.1039/c6cs00062b>.
- [7] J. Zhou, J. Li, L. Kan, L. Zhang, Q. Huang, Y. Yan, Y. Chen, J. Liu, S.-L. Li, Y.-Q. Lan, Linking oxidative and reductive clusters to prepare crystalline porous catalysts for photocatalytic CO_2 reduction with H_2O , *Nat. Commun.* 13 (2022) 4681, <https://doi.org/10.1038/s41467-022-32449-z>.
- [8] A.M. Idris, T. Liu, J. Hussain Shah, H. Han, C. Li, $\text{Sr}_2\text{CoTaO}_6$ double perovskite oxide as a novel visible-light-absorbing bifunctional photocatalyst for photocatalytic oxygen and hydrogen evolution reactions, *ACS Sustain. Chem. Eng.* 8 (2020) 14190–14197, <https://doi.org/10.1021/acssuschemeng.0c05237>.
- [9] A.M. Idris, T. Liu, J. Hussain Shah, A.S. Malik, D. Zhao, H. Han, C. Li, Sr_2NiWO_6 double perovskite oxide as a novel visible-light-responsive water oxidation photocatalyst, *ACS Appl. Mater. Interfaces* 12 (2020) 25938–25948, <https://doi.org/10.1021/acsmi.0c05576>.
- [10] L. Xiong, J. Tang, Strategies and challenges on selectivity of photocatalytic oxidation of organic substances, *Adv. Energy Mater.* 11 (2021) 2003216, <https://doi.org/10.1002/aenm.202003216>.
- [11] X. Cao, Z. Chen, R. Lin, W.-C. Cheong, S. Liu, J. Zhang, Q. Peng, C. Chen, T. Han, X. Tong, Y. Wang, R. Shen, W. Zhu, D. Wang, Y. Li, A photochromic composite with enhanced carrier separation for the photocatalytic activation of benzylic C-H bonds in toluene, *Nat. Catal.* 1 (2018) 704–710, <https://doi.org/10.1038/s41929-018-0128-z>.
- [12] L. Chen, J. Tang, L.-N. Song, P. Chen, J. He, C.-T. Au, S.-F. Yin, Heterogeneous photocatalysis for selective oxidation of alcohols and hydrocarbons, *Appl. Catal. B-Environ.* 242 (2019) 379–388, <https://doi.org/10.1016/j.apcatb.2018.10.025>.
- [13] X. Yang, S. Zhang, P. Li, S. Gao, R. Cao, Visible-light-driven photocatalytic selective organic oxidation reactions, *J. Mater. Chem. A* 8 (2020) 20897–20924, <https://doi.org/10.1039/d0ta05485b>.
- [14] X. Lang, X. Chen, J. Zhao, Heterogeneous visible light photocatalysis for selective organic transformations, *Chem. Soc. Rev.* 43 (2014) 473–486, <https://doi.org/10.1039/c3cs60188a>.
- [15] L. Yuan, M.Y. Qi, Z.R. Tang, Y.J. Xu, Coupling strategy for CO_2 valorization integrated with organic synthesis by heterogeneous photocatalysis, *Angew. Chem. Int. Ed.* 60 (2021) 2–25, <https://doi.org/10.1002/ange.202101667>.
- [16] H. Liu, H.-L. Jiang, Solar-powered artificial photosynthesis coupled with organic synthesis, *Chem* 5 (2019) 2508–2510, <https://doi.org/10.1016/j.chempr.2019.09.006>.
- [17] Y. Cao, X. He, N. Wang, H.R. Li, L.N. He, Photochemical and electrochemical carbon dioxide utilization with organic compounds, *Chin. J. Chem.* 36 (2018) 644–659, <https://doi.org/10.1002/cjoc.201700742>.
- [18] T. Kong, Y. Jiang, Y. Xiong, Photocatalytic CO_2 conversion: What can we learn from conventional CO_x hydrogenation? *Chem. Soc. Rev.* 49 (2020) 6579–6591, <https://doi.org/10.1039/c9cs00920e>.
- [19] H. Huang, J. Zhao, Y. Du, C. Zhou, M. Zhang, Z. Wang, Y. Weng, J. Long, J. Hofkens, J.A. Steele, M.B.J. Roeffaers, Direct Z-scheme heterojunction of semicoherent $\text{FAPbBr}_3/\text{Bi}_2\text{WO}_6$ interface for photoredox reaction with large driving force, *ACS Nano* 14 (2020) 16689–16697, <https://doi.org/10.1021/acsnano.0c03146>.
- [20] Z. Chen, M.Z. Shahid, X. Jiang, M. Zhang, D. Pan, H. Xu, G. Jiang, J. Wang, Z. Li, Regulating the active sites of $\text{Cs}_2\text{AgBiCl}_6$ by doping for efficient coupling of photocatalytic CO_2 reduction and benzyl alcohol oxidation, *Small* 20 (2023) 2304756, <https://doi.org/10.1002/smll.202304756>.
- [21] S. Bai, J. Jiang, Q. Zhang, Y. Xiong, Steering charge kinetics in photocatalysis: intersection of materials syntheses, characterization techniques and theoretical simulations, *Chem. Soc. Rev.* 44 (2015) 2893–2939, <https://doi.org/10.1039/c5cs0064e>.
- [22] J. Low, J. Yu, M. Jaroniec, S. Wageh, A.A. Al-Ghamdi, Heterojunction photocatalysts, *Adv. Mater.* 29 (2017) 1601694, <https://doi.org/10.1002/adma.201601694>.
- [23] H. Yu, M. Dai, J. Zhang, W. Chen, Q. Jin, S. Wang, Z. He, Interface engineering in 2D/2D heterogeneous photocatalysts, *Small* 19 (2023) e2205767, <https://doi.org/10.1002/smll.202205767>.
- [24] Q. Xu, L. Zhang, B. Cheng, J. Fan, J. Yu, S-Scheme heterojunction photocatalyst, *Chem* 6 (2020) 1543–1559, <https://doi.org/10.1016/j.chempr.2020.06.010>.
- [25] J. Fu, Q. Xu, J. Low, C. Jiang, J. Yu, Ultrathin 2D/2D $\text{WO}_3/\text{g-C}_3\text{N}_4$ step-scheme H_2 -production photocatalyst, *Appl. Catal. B-Environ.* 243 (2019) 556–565, <https://doi.org/10.1016/j.apcatb.2018.11.011>.
- [26] Z.F. Huang, J. Song, X. Wang, L. Pan, K. Li, X. Zhang, L. Wang, J.-J. Zou, Switching charge transfer of $\text{Cs}_2\text{Na}/\text{W}_{18}\text{O}_{49}$ from type-II to Z-scheme by interfacial band bending for highly efficient photocatalytic hydrogen evolution, *Nano Energy* 40 (2017) 308–316, <https://doi.org/10.1016/j.nanoen.2017.08.032>.
- [27] J. Zhou, B. Gao, D. Wu, C. Tian, H. Ran, W. Chen, Q. Huang, W. Zhang, F. Qi, N. Zhang, Y. Pu, J. Qiu, Z. Hu, J. Du, Z. Liu, Y. Leng, X. Tang, Enhanced photocatalytic activity of lead-free $\text{Cs}_2\text{TeBr}_6/\text{g-C}_3\text{N}_4$ heterojunction photocatalyst and its mechanism, *Adv. Funct. Mater.* (2023) 2308411, <https://doi.org/10.1002/adfm.202308411>.
- [28] L. Zhang, J. Zhang, H. Yu, J. Yu, Emerging S-scheme photocatalyst, *Adv. Mater.* 34 (2022) e2107668, <https://doi.org/10.1002/adma.202107668>.
- [29] R. Shi, G.I.N. Waterhouse, T. Zhang, Recent progress in photocatalytic CO_2 reduction over perovskite oxides, *Sol. RRL* 1 (2017) 1700126, <https://doi.org/10.1002/solr.201700126>.
- [30] X. Yue, L. Cheng, J. Fan, Q. Xiang, 2D/2D $\text{BiVO}_4/\text{CsPbBr}_3$ S-scheme heterojunction for photocatalytic CO_2 reduction: Insights into structure regulation and Fermi level modulation, *Appl. Catal. B-Environ.* 304 (2022) 120979, <https://doi.org/10.1016/j.apcatb.2021.120979>.
- [31] C. Xu, Y. Pan, G. Wan, H. Liu, L. Wang, H. Zhou, S.H. Yu, H.L. Jiang, Turning on visible-light photocatalytic C-H oxidation over metal-organic frameworks by introducing metal-to-cluster charge transfer, *J. Am. Chem. Soc.* 141 (2019) 19110–19117, <https://doi.org/10.1021/jacs.9b09954>.
- [32] Y.-X. Tan, Z.-M. Chai, B.-H. Wang, S. Tian, X.-X. Deng, Z.-J. Bai, L. Chen, S. Shen, J.-K. Guo, M.-Q. Cai, C.-T. Au, S.-F. Yin, Boosted photocatalytic oxidation of toluene into benzaldehyde on $\text{CdIn}_2\text{S}_4\text{-CdS}$: synergistic effect of compact heterojunction and S-vacancy, *ACS Catal.* 11 (2021) 2492–2503, <https://doi.org/10.1021/acscatal.0c05703>.
- [33] H. Zhang, Y. Wang, S. Zuo, W. Zhou, J. Zhang, X.W.D. Lou, Isolated cobalt centers on $\text{W}_{18}\text{O}_{49}$ nanowires perform as a reaction switch for efficient CO_2 photoreduction, *J. Am. Chem. Soc.* 143 (2021) 2173–2177, <https://doi.org/10.1021/jacs.0c08409>.
- [34] N. Zhang, A. Jalil, D. Wu, S. Chen, Y. Liu, C. Gao, W. Ye, Z. Qi, H. Ju, C. Wang, X. Wu, L. Song, J. Zhu, Y. Xiong, Refining defect states in $\text{W}_{18}\text{O}_{49}$ by Mo doping: a strategy for tuning N_2 activation towards solar-driven nitrogen fixation, *J. Am. Chem. Soc.* 140 (2018) 9434–9443, <https://doi.org/10.1021/jacs.8b02076>.
- [35] H. Bai, W. Yi, J. Liu, Q. Lv, Q. Zhang, Q. Ma, H. Yang, G. Xi, Large-scale synthesis of ultrathin tungsten oxide nanowire networks: an efficient catalyst for aerobic oxidation of toluene to benzaldehyde under visible light, *Nanoscale* 8 (2016) 13545–13551, <https://doi.org/10.1039/c6nr02949c>.
- [36] Z. Yang, S. Peng, F. Lin, P. Wang, G. Xing, L. Yu, Self-assembly behavior of metal halide perovskite nanocrystals, *Chin. J. Chem.* 40 (2022) 2239–2248, <https://doi.org/10.1002/cjoc.202200161>.
- [37] J. Liu, O. Margeat, W. Dachraoui, X. Liu, M. Fahlman, J. Ackermann, Gram-scale synthesis of ultrathin tungsten oxide nanowires and their aspect ratio-dependent photocatalytic activity, *Adv. Funct. Mater.* 24 (2014) 6029–6037, <https://doi.org/10.1002/adfm.201401261>.
- [38] S. Wan, M. Ou, Q. Zhong, X. Wang, Perovskite-type CsPbBr_3 quantum dots/ $\text{UiO}-66$ (NH_2) nanojunction as efficient visible-light-driven photocatalyst for CO_2 reduction, *Chem. Eng. J.* 358 (2019) 1287–1295, <https://doi.org/10.1016/j.cej.2018.10.120>.
- [39] M. Li, X. Zhang, P. Yang, Controlling the growth of a SiO_2 coating on hydrophobic CsPbBr_3 nanocrystals towards aqueous transfer and high luminescence, *Nanoscale* 13 (2021) 3860–3867, <https://doi.org/10.1039/d0nr08325a>.
- [40] P. Makuta, M. Pacia, W. Macyk, How to correctly determine the band gap energy of modified semiconductor photocatalysts based on UV-vis spectra, *J. Phys. Chem. Lett.* 9 (2018) 6814–6817, <https://doi.org/10.1021/acs.jpcllett.8b02892>.
- [41] R. Alcaraz de la Osa, I. Iparragirre, D. Ortiz, J.M. Saiz, The extended Kubelka-Munk theory and its application to spectroscopy, *ChemTexts* 6 (2019) 2, <https://doi.org/10.1007/s40828-019-0097-0>.
- [42] L. Liang, X. Li, Y. Sun, Y. Tan, X. Jiao, H. Ju, Z. Qi, J. Zhu, Y. Xie, Infrared light-driven CO_2 overall splitting at room temperature, *Joule* 2 (2018) 1004–1016, <https://doi.org/10.1016/j.joule.2018.02.019>.
- [43] J. Zhao, Q. Huang, Z. Xie, Y. Liu, F. Liu, F. Wei, S. Wang, Z. Zhang, R. Yuan, K. Wu, Z. Ding, J. Long, Hierarchical hollow $\text{TiO}_2/\text{CdS}/\text{ZnS}$ hybrid for solar-driven CO_2 -selective conversion, *ACS Appl. Mater. Interfaces* 15 (2023) 24494–24503, <https://doi.org/10.1021/acsmi.3c03255>.

[44] L. Wang, B. Cheng, L. Zhang, J. Yu, In situ irradiated XPS investigation on S-Scheme $\text{TiO}_2@\text{ZnIn}_2\text{S}_4$ photocatalyst for efficient photocatalytic CO_2 reduction, *Small* 17 (2021) e2103447, <https://doi.org/10.1002/smll.202103447>.

[45] B. He, P. Xiao, S. Wan, J. Zhang, T. Chen, L. Zhang, J. Yu, Rapid charge transfer endowed by interfacial Ni-O bonding in S-scheme heterojunction for efficient photocatalytic H_2 and imine production, *Angew. Chem. Int. Ed.* 62 (2023) e202313172, <https://doi.org/10.1002/anie.202313172>.

[46] Y. Jiang, H.Y. Chen, J.Y. Li, J.F. Liao, H.H. Zhang, X.D. Wang, D.B. Kuang, Z-Scheme 2D/2D heterojunction of $\text{CsPbBr}_3/\text{Bi}_2\text{WO}_6$ for improved photocatalytic CO_2 reduction, *Adv. Funct. Mater.* 30 (2020) 2004293, <https://doi.org/10.1002/adfm.202004293>.

[47] Q. Lin, S. Tan, J. Zhao, X. Fang, Y. Wang, N. Wen, Z. Zhang, Z. Ding, R. Yuan, G. Yan, S. Jin, J. Long, Tunable band engineering management on perovskite $\text{MAPbBr}_3/\text{COFs}$ nano-heterostructures for efficient S-S coupling reactions, *Small* 20 (2023) 2304776, <https://doi.org/10.1002/smll.202304776>.

[48] X. Jiang, Y. Ding, S. Zheng, Y. Ye, Z. Li, L. Xu, J. Wang, Z. Li, X.J. Loh, E. Ye, L. Sun, In-situ generated CsPbBr_3 nanocrystals on O-defective WO_3 for photocatalytic CO_2 reduction, *ChemSusChem* 15 (2022) e202102295, <https://doi.org/10.1002/cssc.202102295>.

[49] L. Wang, B. Zhu, J. Zhang, J.B. Ghasemi, M. Mousavi, J. Yu, S-scheme heterojunction photocatalysts for CO_2 reduction, *Matter* 5 (2022) 4187–4211, <https://doi.org/10.1016/j.matt.2022.09.009>.

[50] A. Mahmoud Idris, S. Zheng, L. Wu, S. Zhou, H. Lin, Z. Chen, L. Xu, J. Wang, Z. Li, A heterostructure of halide and oxide double perovskites $\text{Cs}_2\text{AgBiBr}_6/\text{Sr}_2\text{FeNbO}_6$ for boosting the charge separation toward high efficient photocatalytic CO_2 reduction under visible-light irradiation, *Chem. Eng. J.* 446 (2022) 137197, <https://doi.org/10.1016/j.cej.2022.137197>.

[51] B.L. Shitong Han, Lijuan Huang, Hailing Xi, Zhengxin Ding, Jinlin Long, Construction of $\text{ZnIn}_2\text{S}_4/\text{CdIn}_2\text{S}_4$ microspheres for efficient photo-catalytic reduction of CO_2 with visible light, *Chin. J. Struct. Chem.* 41 (2022) 2201007–2201013, <https://doi.org/10.14102/j.cnki.0254-5861.2021-0026>.

[52] J. Schneider, D.W. Bahnemann, Undesired role of sacrificial reagents in photocatalysis, *J. Phys. Chem. Lett.* 4 (2013) 3479–3483, <https://doi.org/10.1021/jz4018199>.

[53] R. Hao, G. Wang, H. Tang, L. Sun, C. Xu, D. Han, Template-free preparation of macro/mesoporous $\text{g-C}_3\text{N}_4/\text{TiO}_2$ heterojunction photocatalysts with enhanced visible light photocatalytic activity, *Appl. Catal. B-Environ.* 187 (2016) 47–58, <https://doi.org/10.1016/j.apcatb.2016.01.026>.

[54] Y. Wang, H. Li, Q. Lin, J. Zhao, X. Fang, N. Wen, Z. Zhang, Z. Ding, R. Yuan, X.-H. Huang, J. Long, Nanoscale OD/1D heterojunction of $\text{MAPbBr}_3/\text{COF}$ toward efficient LED-driven S-S coupling reactions, *ACS Catal.* 13 (2023) 15493–15504, <https://doi.org/10.1021/acscatal.3c03051>.

[55] X. Cao, A. Huang, C. Liang, H.-C. Chen, T. Han, R. Lin, Q. Peng, Z. Zhuang, R. Shen, H.M. Chen, Y. Yu, C. Chen, Y. Li, Engineering lattice disorder on a photocatalyst: photochromic BiOBr nanosheets enhance activation of aromatic C-H bonds via water oxidation, *J. Am. Chem. Soc.* 144 (2022) 3386–3397, <https://doi.org/10.1021/jacs.1c10112>.

[56] M. Zhang, Y. Mao, X. Bao, G. Zhai, D. Xiao, D. Liu, P. Wang, H. Cheng, Y. Liu, Z. Zheng, Y. Dai, Y. Fan, Z. Wang, B. Huang, Coupling benzylamine oxidation with CO_2 photoconversion to ethanol over a black phosphorus and bismuth tungstate S-scheme heterojunction, *Angew. Chem. Int. Ed.* 62 (2023) e202302919, <https://doi.org/10.1002/anie.202302919>.

[57] Y. Deng, C. Wan, C. Li, Y. Wang, X. Mu, W. Liu, Y. Huang, P.K. Wong, L. Ye, Synergy effect between facet and zero-valent copper for selectivity photocatalytic methane formation from CO_2 , *ACS Catal.* 12 (2022) 4526–4533, <https://doi.org/10.1021/acscatal.2c00167>.

[58] X. Ren, M. Gao, Y. Zhang, Z. Zhang, X. Cao, B. Wang, X. Wang, Photocatalytic reduction of CO_2 on BiO_x : effect of halogen element type and surface oxygen vacancy mediated mechanism, *Appl. Catal. B-Environ.* 274 (2020) 119063, <https://doi.org/10.1016/j.apcatb.2020.119063>.

[59] X. Zu, Y. Zhao, X. Li, R. Chen, W. Shao, L. Li, P. Qiao, W. Yan, Y. Pan, Q. Xu, J. Zhu, Y. Sun, Y. Xie, Reversible switching $\text{Cu}^{\text{II}}/\text{Cu}^{\text{I}}$ single sites catalyze high-rate and selective CO_2 photoreduction, *Angew. Chem. Int. Ed.* 62 (2022) e202215247, <https://doi.org/10.1002/anie.202215247>.

[60] K. Zhang, H. Chen, Y. Liu, J. Deng, L. Jing, A. Rastegarpanah, W. Pei, Z. Han, H. Dai, Two-dimensional $\text{Bi}_2\text{W}_{x}\text{Mo}_{1-x}\text{O}_6$ solid solution nanosheets for enhanced photocatalytic toluene oxidation to benzaldehyde, *Appl. Catal. B-Environ.* 315 (2022) 121545, <https://doi.org/10.1016/j.apcatb.2022.121545>.

[61] S. Zhu, B. Jiang, W.-B. Cai, M. Shao, Direct observation on reaction intermediates and the role of bicarbonate anions in CO_2 electrochemical reduction reaction on Cu surfaces, *J. Am. Chem. Soc.* 139 (2017) 15664–15667, <https://doi.org/10.1021/jacs.7b10462>.

[62] Z. Miao, Q. Wang, Y. Zhang, L. Meng, X. Wang, In situ construction of S-scheme AgBr/BiOBr heterojunction with surface oxygen vacancy for boosting photocatalytic CO_2 reduction with H_2O , *Appl. Catal. B-Environ.* 301 (2022) 120802, <https://doi.org/10.1016/j.apcatb.2021.120802>.

[63] W. Wang, C. Deng, S. Xie, Y. Li, W. Zhang, H. Sheng, C. Chen, J. Zhao, Photocatalytic C-C coupling from carbon dioxide reduction on copper oxide with mixed-valence copper(I)/copper(II), *J. Am. Chem. Soc.* 143 (2021) 2984–2993, <https://doi.org/10.1021/jacs.1c00206>.

[64] X. Li, T. Wang, X. Tao, G. Qiu, C. Li, B. Li, Interfacial synergy of Pd sites and defective BiOBr for promoting the solar-driven selective oxidation of toluene, *J. Mater. Chem. A* 8 (2020) 17657–17669, <https://doi.org/10.1039/d0ta05733a>.

[65] H. Li, F. Qin, Z. Yang, X. Cui, J. Wang, L. Zhang, New reaction pathway induced by plasmon for selective benzyl alcohol oxidation on BiOCl possessing oxygen vacancies, *J. Am. Chem. Soc.* 139 (2017) 3513–3521, <https://doi.org/10.1021/jacs.6b12850>.

[66] J. Zhao, Z. Miao, Y. Zhang, G. Wen, L. Liu, X. Wang, X. Cao, B. Wang, Oxygen vacancy-rich hierarchical BiOBr hollow microspheres with dramatic CO_2 photoreduction activity, *J. Colloid Interface Sci.* 593 (2021) 231–243, <https://doi.org/10.1016/j.jcis.2021.02.117>.

[67] Q. Wang, Z. Miao, Y. Zhang, T. Yan, L. Meng, X. Wang, Photocatalytic reduction of CO_2 with H_2O mediated by Ce-Tailored bismuth oxybromide surface frustrated lewis pairs, *ACS Catal.* 12 (2022) 4016–4025, <https://doi.org/10.1021/ascatal.1c05553>.

[68] P. Zhang, X. Sui, Y. Wang, Z. Wang, J. Zhao, N. Wen, H. Chen, H. Huang, Z. Zhang, R. Yuan, Z. Ding, W. Dai, X. Fu, Y.-X. Weng, J. Long, Surface Ru-H bipyridine complexes-grafted TiO_2 nanohybrids for efficient photocatalytic CO_2 methanation, *J. Am. Chem. Soc.* 145 (2023) 5769–5777, <https://doi.org/10.1021/jacs.2c12632>.

[69] K. Wang, J. Li, X. Liu, Q. Cheng, Y. Du, D. Li, G. Wang, B. Liu, Sacrificial-agent-free artificial photosynthesis of hydrogen peroxide over step-scheme WO_3/NiS hybrid nanofibers, *Appl. Catal. B-Environ.* 342 (2024) 123349, <https://doi.org/10.1016/j.apcatb.2023.123349>.

[70] X.-M. Gao, F. Fu, L.-P. Zhang, W.-H. Li, The preparation of Ag-BiVO_4 metal composite oxides and its application in efficient photocatalytic oxidative thiophene, *Phys. B Condens. Matter* 419 (2013) 80–85, <https://doi.org/10.1016/j.physb.2013.03.024>.

[71] K. Xie, H. Zhang, S. Sun, Y. Gao, Functions of boric acid in fabricating TiO_2 for photocatalytic degradation of organic contaminants and hydrogen evolution, *Mol. Catal.* 479 (2019) 110614, <https://doi.org/10.1016/j.mcat.2019.110614>.